Recent Advances in the BiVO4 Photocatalyst for Sun-Driven Water Oxidation: Top-Performing Photoanodes and Scale-Up Challenges

catalysts

MDPI

Review

Recent Advances in the $BiVO_4$ Photocatalyst for Sun-Driven Water Oxidation: Top-Performing Photoanodes and Scale-Up Challenges

Kristine Rodulfo Tolod [1,2], Simelys Hernández [1,3,*] and Nunzio Russo [1]

[1] Politecnico di Torino, Corso Duca degli Abruzzi, 10129 Turin, Italy; kristine.tolod@polito.it (K.R.T.); nunzio.russo@polito.it (N.R.)
[2] Ecole Doctorale de Chimie, Université Claude Bernard Lyon 1, Villeurbanne Cedex, 69622 Lyon, France
[3] Center for Sustainable Future Technologies (CSF@POLITO), Istituto Italiano di Tecnologia, 10129 Turin, Italy
* Correspondence: simelys.hernandez@polito.it; Tel.: +39-011-090-4774

Academic Editor: Yurii V. Geletii
Received: 24 November 2016; Accepted: 28 December 2016; Published: 1 January 2017

Abstract: Photoelectrochemical (PEC) water splitting, which is a type of artificial photosynthesis, is a sustainable way of converting solar energy into chemical energy. The water oxidation half-reaction has always represented the bottleneck of this process because of the thermodynamic and kinetic challenges that are involved. Several materials have been explored and studied to address the issues pertaining to solar water oxidation. Significant advances have recently been made in the use of stable and relatively cheap metal oxides, i.e., semiconducting photocatalysts. The use of $BiVO_4$ for this purpose can be considered advantageous because this catalyst is able to absorb a substantial portion of the solar spectrum and has favourable conduction and valence band edge positions. However, $BiVO_4$ is also associated with poor electron mobility and slow water oxidation kinetics and these are the problems that are currently being investigated in the ongoing research in this field. This review focuses on the most recent advances in the best-performing $BiVO_4$-based photoanodes to date. It summarizes the critical parameters that contribute to the performance of these photoanodes, and highlights so far unresolved critical features related to the scale-up of a $BiVO_4$-based PEC water-splitting device.

Keywords: solar fuels; water oxidation; $BiVO_4$ photoanode; artificial photosynthesis; tandem cells

1. Introduction

Photoelectrochemical (PEC) water splitting is an alternative way of directly producing solar fuels, that is, hydrogen and oxygen, from water. This process often makes use of semiconductor photoelectrodes to convert solar energy to chemical energy [1,2], thus, enabling the abundant but intermittent solar energy to be harvested, stored and converted into a form that can be stored easily.

In order to efficiently and sustainably split water into hydrogen and oxygen, several material requirements have to be met simultaneously [3,4]: (1) a sufficient photo-voltage and an appropriate band alignment to split the water; (2) substantial absorption of the solar spectrum, which prevalently consists of visible light; (3) efficient and fast transport of the charges between the semiconductor and the electrolyte solution; and (4) stability and cost-effectiveness. The search for suitable materials that can satisfy these requirements is the focus of the current on-going studies on photocatalysts [5].

PEC water splitting, which is a form of artificial photosynthesis, has been studied extensively since it was first reported by Fujishima and Honda in 1972 [6], when they used a TiO_2 photoanode and a Pt cathode to demonstrate the process by irradiating a photoanode with UV light. It is well

known that the bottleneck of this process lies in the water oxidation half reaction, which produces oxygen [7,8]. The water oxidation reaction causes a bottleneck because, as shown in Equation (1),

$$\begin{gathered} 2H_2O \Leftrightarrow O_2 + 4H^+ + 4e^- \\ \mathbf{4H^+ + 4e^- \Leftrightarrow 2H_2} \\ \mathbf{2H_2O \rightarrow 2H_2 + O_2} \end{gathered} \quad (1)$$

it is a 4-electron oxidation process of two water molecules coupled with the removal of four protons, to produce a weak oxygen-oxygen bond [9]. Since a photochemical process would be necessary for water splitting to take place, there is still a need for accumulated stepwise one-electron transfers under very specific photon-flux-density conditions. The challenge lies in the difficulty involved in preserving an oxidized state in a desired microenvironment and in avoiding its quenching as it awaits the arrival of the next photon [10].

Several studies have been conducted to evaluate appropriate materials that can serve as efficient photoanodes in order to overcome this bottleneck [11–14]. The focus of this review is on the use of $BiVO_4$ photoanodes for solar water oxidation.

1.1. $BiVO_4$ as a Photoanode

Metal oxides [15,16], such as $BiVO_4$, are the preferred materials for photoanodes, because of their ability to withstand oxidizing conditions and because of their general low-cost [4]. Compared to other metal oxides, the difference between the valence and the conduction band edge positions of $BiVO_4$ is more strategic and relatively low (~2.4 eV), and, it therefore requires less bias potential.

$BiVO_4$ was first synthesized by Roth and Waring in 1963 via solid state and melting reactions [17]. Interest in the study of $BiVO_4$ was initially due to the ferroelastic properties of the material, and its ferroelastic-paraelastic transition reported at 528 K (255 °C) [18], a property that depends on the crystal structure. $BiVO_4$ has three main crystal forms: a monoclinic scheelite, a tetragonal zircon-type and a tetragonal scheelite structures [18,19]. An irreversible transition from the tetragonal zircon-type to the monoclinic scheelite structure occurs at calcination temperatures of about 400–500 °C. Moreover, a reversible transition occurs between the monoclinic-scheelite and the tetragonal scheelite structures at a temperature of 255 °C, the same temperature that is responsible for the ferroelastic-paraelastic transition. Apart from temperature-induced transitions, it has also been reported that mechanical grinding at room temperature could irreversibly transform the tetragonal structure into a monoclinic structure [20]. Of the three $BiVO_4$ crystal structures, the monoclinic scheelite structure is the one that is most commonly used for photocatalysis because of its higher activity than the other structures [5].

The Bi in monoclinic scheelite $BiVO_4$ is coordinated to O in a distorted oxygen octahedron, while V is the centre of a distorted oxygen tetrahedron, thus implying oxidation states of Bi^{3+} ($5d^{10}6s^2$), V^{5+} ($3d^0$), and O^{2-} ($2p^6$), according to Walsh et al. [21]. Moreover, the valence band mainly consists of O 2p, coupled to Bi 6s, while the conduction band is dominantly constituted by V 3d states, with contributions from the O 2p and Bi 6p states [21,22]. These couplings result in an upward dispersion of the valence band, and a lowering of the conduction band to a minimum, thereby causing symmetric electron and hole masses, which facilitate a relatively efficient charge carrier separation and extraction. As far as its calculated optical absorption spectrum is concerned, it has been reported that the fundamental band-edge transitions are dipole-allowed, beginning at 2.1 eV and with peaks at 2.4 eV, and thus display absorption in the visible light range. Cooper et al. [22] stated that the poor electron mobility of $BiVO_4$ could be a consequence of the localization of the V 3d orbitals in the conduction band minimum, due to its poor overlapping with the Bi 6p orbitals.

In 1998, Kudo et al. [23] first reported the photoactivity of a $BiVO_4$ powder for the water splitting reaction and measured the production of O_2, under visible light irradiation, in the presence of Ag^+ that was used as a hole scavenger. This opened up a whole new era in which the potential of $BiVO_4$ has been explored as a photoanode.

1.1.1. Advantages of $BiVO_4$ as a Photoanode

$BiVO_4$ has a relatively low band gap energy of 2.4 eV, which makes it capable of readily absorbing visible light [23,24]. Therefore, its theoretical maximum photocurrent density is 7.5 mA/cm^2 [25]. Assuming all the photons with energies above 2.4 eV are absorbed, the result is a 9% Solar-to-Hydrogen (STH) efficiency [26].

Moreover, the conduction band edge position of $BiVO_4$ is favourably located, because it almost coincides with the thermodynamic hydrogen evolution potential [19,27]. This promotes an earlier photocurrent onset and the generation of a higher photocurrent in the low bias region than other photoanodes [28]. These factors are essential to attain a high overall operating current and could eventually lead to a higher STH efficiency [29].

Finally, $BiVO_4$ is an inexpensive and nontoxic material that is composed of earth-abundant elements. In fact, it has been estimated that 135 ppm of vanadium and 0.17 ppm of bismuth are present in the earth's continental crust [30]. In general, like most metal oxides, it is also known to be stable against chemical corrosion [31,32].

1.1.2. Disadvantages of $BiVO_4$ as a Photoanode

The use of $BiVO_4$ as a photoanode also involves some drawbacks. $BiVO_4$ is known to suffer from poor electron mobility, and photon efficiency is therefore lost relatively easily to electron-hole recombination [33,34]. This phenomenon is reportedly due to the fact that the VO_4 tetrahedra are not connected to each other [35], thus making it hard for photogenerated electrons to flow towards the conducting support.

In addition, in order to maximize the photogeneration of charges, the thickness of the material has to be optimized according to the optical penetration depth [3]. However, $BiVO_4$ has a short hole diffusion length, estimated as 70–100 nm [36,37], which compromises and restricts the necessary light penetration depth.

Finally, $BiVO_4$ is known to exhibit poor water oxidation kinetics, and this constitutes a bottleneck that still has to be overcome in the design of photoanodes.

This review paper deals with the top-performing $BiVO_4$-based photoanodes, and discusses the significant properties and strategies that have been applied to improve their performances. The aim has been to analyse the still remaining critical issues, in order to guide the necessary developments, and to achieve a high-scale PEC reactor based on a $BiVO_4$ photoanode for solar fuel production.

2. Top-Performing $BiVO_4$-Based Photoanodes

The best-performing photoanodes that have been produced to date have been made via a combination of several techniques that address the electron mobility and water oxidation kinetics issues that are discussed in the following sections.

Figure 1 summarizes the recently produced $BiVO_4$-based photoanodes that have exhibited the best performances in terms of photocurrent densities. All the photocurrent densities that are reported hereafter refer to standard conditions, with an illumination of AM 1.5 G, an intensity of 1 sun (100 mW/cm^2), and measurement at about 1.23 V vs. RHE (reversible hydrogen electrode).

To date, the best photoanode reported is the $WO_3/BiVO_4$ core-shell nanorod structure with Co-Pi, which was synthesized by Pihosh et al. [38], and which yielded a photocurrent density of 6.72 mA/cm^2 at 1.23 V vs. RHE. The WO_3 layer was synthesized via glancing angle deposition (GLAD), the $BiVO_4$ via electrodeposition and the cobalt phosphate (Co-Pi) oxygen evolution catalyst (OEC) was added via a photo-assisted electrodeposition. More details on the performance, correlated to the different properties of these materials, are given in the following sections.

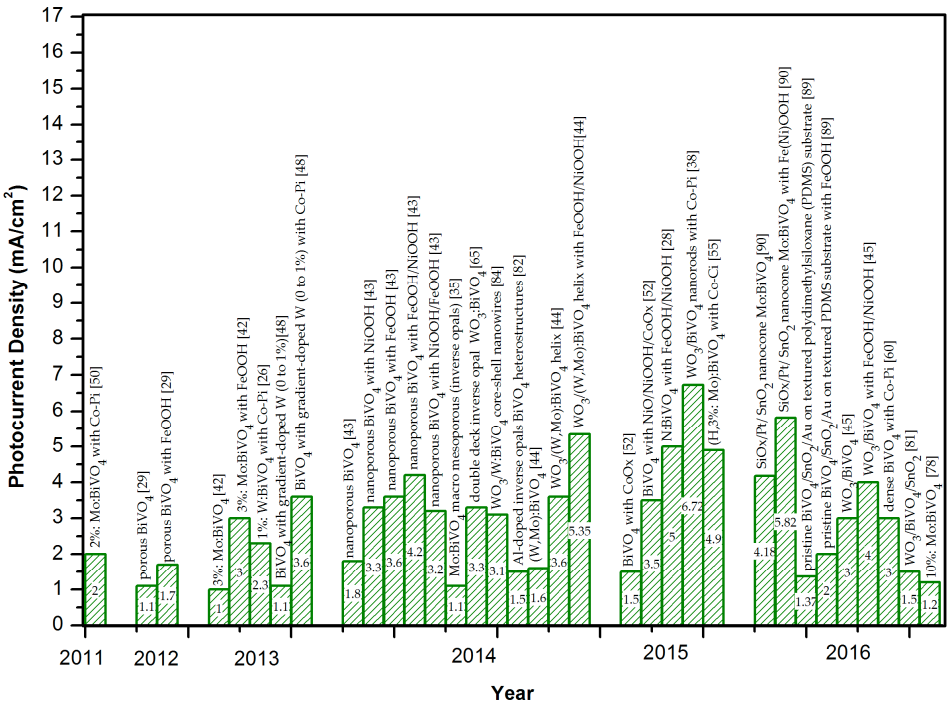

Figure 1. Top-performing $BiVO_4$-based photoanodes from 2011 to 2016 (measured at a standard illumination of AM 1.5 G, and an intensity of 1 sun (100 mW/cm^2), obtained at 1.2–1.23 V vs. RHE).

2.1. Strategies Adopted to Enhance Reaction Kinetics in Solar Water Oxidation

Oxygen evolution catalysts (OECs) have brought about huge improvements in the photocurrent density, as they reduce the kinetic barrier of water oxidation and provide unique catalytically active sites with specific selectivity [39]. They promote the negative shift of the overpotential, which leads to the necessity of less external energy to achieve photoelectrochemical water oxidation [40].

As is evident from the photoanodes presented in Figure 1, OECs are used in top-performing $BiVO_4$ photoanodes to address the issue of poor water oxidation kinetics. Noticeable efforts have been made to work with non-noble metals and earth-abundant materials as OEC materials.

The use of FeOOH as an OEC for $BiVO_4$ has shown an outstanding performance in the low-bias region, as reported by Seabold and Choi [41]. A photocurrent density of 1 mA/cm^2 was achieved with $BiVO_4$/FeOOH electrodes at an applied potential as low as 0.5 V vs. RHE, as the best result, and at 0.6 V vs. RHE on average, operating at a neutral pH condition in a phosphate electrolyte. In the presence of FeOOH, the photocurrent onset was shifted by 0.5 V towards the flat band potential. This is an important feature in the assembly of a complete photoelectrochemical cell, because it affects the overall operating current density. In addition, a photocurrent density of 1.7 mA/cm^2 at 1.2 V vs. RHE was obtained and maintained for 6 h, with only 2% of decay with FeOOH in comparison to the significant decrease in photocurrent observed within a few minutes for the bare $BiVO_4$. This suggests that the FeOOH layer induced the photostability of $BiVO_4$/FeOOH. The use of FeOOH has been replicated in other studies for these reasons [29,42].

Kim and Choi have shown that the use of NiOOH, as an OEC for $BiVO_4$, exhibits an earlier photocurrent onset of 0.26 V vs. RHE versus the 0.31 V vs. RHE that was obtained for $BiVO_4$/FeOOH. The authors also confirmed that $BiVO_4$/NiOOH has a more negative flat band potential than $BiVO_4$/FeOOH. However, a photocurrent density of 1.8 mA/cm^2 at 0.6 V vs. RHE (3.3 mA/cm^2 at 1.23 V vs. RHE) has been reported for $BiVO_4$/NiOOH, a value which falls below the 2.2 mA/cm^2 at 0.6 V vs. RHE (3.6 mA/cm^2 at 1.23 V vs. RHE) for $BiVO_4$/FeOOH (all operated and measured at neutral pH conditions in a phosphate electrolyte). In the same study, Kim and Choi reported that an optimum dual OEC structure with FeOOH/NiOOH used in series is responsible for the simultaneous

optimization of the $BiVO_4$/OEC and OEC/electrolyte junction [28,43]. A similar dual OEC structure was employed by Shi et al. [44,45] to produce high performing $BiVO_4$ photoanodes.

The in situ production of Co-Pi as an OEC was first introduced by Kanan and Nocera [46]. Oxygen is generated at neutral pH using Co-Pi, under atmospheric pressure and room temperature. Co-Pi OEC also demonstrates a self-healing nature in the presence of phosphate, which should ensure the long-term stability of the catalyst system [47]. A 2-fold increase in photocurrent density and a 0.15 V vs. RHE cathodic shift for the onset potential was reported by Abdi et al. [48]. Up to a 7-fold increase in photocurrent density was also reported, following the use of Co-Pi [40,49–51]. Zhong et al. [51] reported a low onset potential of 0.35 V vs. RHE for Co-Pi/W:$BiVO_4$, which seems very promising for use in tandem PEC cells.

Zhong et al. [52], in a different work, introduced CoO_x as an OEC; it was found to be responsible for an increase in the photocurrent density of bare $BiVO_4$ from about 1 mA/cm^2 to about 1.5 mA/cm^2 at 1.2 V vs. RHE, when operating at neutral pH in a phosphate electrolyte. The same authors then used the dual OECs NiOOH (deposited in situ)/CoO_x with an ultrathin ALD-deposited NiO layer on top and added them to a $BiVO_4$/Ti layer. This process was reported to triple the photocurrent density at 0.6 V vs. RHE, yielding up to 3.5 mA/cm^2 at 1.23 V vs. RHE photocurrent density, when operating at neutral pH in a phosphate electrolyte. The NiO was responsible for passivating the $BiVO_4$ surface states, with a consequent enhanced charge separation.

Joya et al. [53] reported the use of a cobalt carbonate (Co-Ci) OEC produced in situ, generated from a CO_2 saturated bicarbonate solution containing Co^{2+} ions. They reported that the Co-Ci OEC in a HCO_3^-/CO_2 electrolyte showed a stable current density of >2 mA/cm^2 at 1.35 V vs. NHE (normal hydrogen electrode), and remained active for 16 h. It was also reported that Co-based OECs, such as Co-Pi and Co-Ci, tend to lose stability in a phosphate electrolyte system during anodic water oxidation, although, they also exhibit a sustained current density and higher stability in a HCO_3^-/CO_2 system. Using the same OEC system at neutral pH, Jin Hyun Kim et al. [54] reported a shift in the onset potential after adding Co-Ci to a $BiVO_4/WO_3$ photoelectrode, that is, from 0.5 V vs. RHE to 0.2 V vs. RHE. The Co-Ci/$BiVO_4/WO_3$ material yielded a photocurrent density of 3.5 mA/cm^2 at 1.23 V vs. RHE, which was higher than the 2.5 mA/cm^2 produced at the same potential by the $BiVO_4/WO_3$ without any OEC. In another work, Jin Hyun Kim et al. [55] used the same OEC in a tandem cell assembly, using a H and 3% Mo co-doped $BiVO_4$ photoanode, which yielded a photocurrent density of 4.8 mA/cm^2 at 1.23 V vs. RHE, and then increased to 5 mA/cm^2 at 1.23 V vs. RHE when enhanced by Co-Ci. This performance was similar to that of Co-Pi, but with a notable increase in stability.

In the OECs discussed above, it is important to note that most of the photoelectrochemical tests were conducted using neutral pH electrolytes. This is an important aspect for $BiVO_4$-based photoanodes, because $BiVO_4$ gradually dissolves into the solution at extreme pH conditions during long-time experiments. Furthermore, neutral pH conditions means less corrosivity of materials and other components of the system, although maintaining a high activity under neutral pH environment has been difficult to be proved. Thus, it is also essential to understand the stability of these OECs in different pH environments.

The electrocatalytic stability of OECs, such as CoO_x, Co-Pi, $CoFeO_x$, IrO_x, NiO_x, $NiCeO_x$, $NiCoO_x$, $NiCuO_x$, $NiFeO_x$, and $NiLaO_x$ has been tested in the OEC benchmarking procedures discussed in the work of McCrory et al. [56,57]. These OECs were placed in both alkaline (1 M NaOH) and acidic (1 M H_2SO_4) environments, and held at a constant current density of 10 mA/cm^2 for 2 h at a 1600 rpm rotation rate while measuring the operating potential as a time function. Most of the catalysts exhibited stable operations in alkaline conditions, showing only < 0.03 V shifts in overpotential, except for $CoFeO_x$ and IrO_x due to catalyst dissolution and loss of material, respectively. Only the IrO_x exhibited a stable operating overpotential of 0.27–0.30 V for 2 h in acidic conditions. All the other OECs exhibited a dramatic increase in the overpotential after just a few minutes, thus indicating their instability. The activity of other OECs, such as PdO_2 [39], Pt [44], Mn_2O_3 [58], and CoO [59] has also been demonstrated in various studies, although their long-term stability has not yet been proved.

In order to address the poor electron mobility issue using $BiVO_4$ as a photoanode in a PEC water splitting system, several strategies have been employed to improve the intrinsic photocurrent density that can be achieved by this material. The $BiVO_4$ photoanode has continuously been altered through the different strategies, with the aim of improving its surface properties, enhancing the electron transport mobility, and ultimately reducing the undesired electron-hole recombination. The most successful of these strategies are described in Section 2.2.

2.2. Strategies Adopted to Enhance the Electron Mobility in Solar Water Oxidation

2.2.1. Morphology Control

Effect of Porosity and the Synthesis Procedure

Bare porous $BiVO_4$ [29] and bare nanoporous $BiVO_4$ [43] films have been synthesized via electrodeposition, and have yielded photocurrent densities of 1.1 mA/cm^2 and 1.8 mA/cm^2 at 1.23 V vs. RHE, respectively. The porosity of the material, which induces a higher surface area, increases the volume of the depletion layer in the semiconductor and improves the electron-hole separation [29]. Improvements in photocurrent densities of 1.7 mA/cm^2 and 4.2 mA/cm^2 (at 1.23 V vs. RHE), respectively, have been reported for each of these materials after addition of an FeOOH O_2 evolution reaction (OER) co-catalyst to the bare porous $BiVO_4$ and of an FeOOH/NiOOH OER co-catalyst to the bare nanoporous $BiVO_4$.

Figure 2a shows an example of porous $BiVO_4$ that the authors synthesized using the electrodeposition route of Kim and Choi [43]. An increased porosity was achieved on a F-doped Tin Oxide (FTO) conductive surface, via the cathodic electrodeposition of BiOI, which served as the bismuth precursor. The thin 2D structure of BiOI gave rise to a porous $BiVO_4$ structure upon calcination, while in contact with vanadium precursors.

In another study by Hernández et al. [60], dense and porous $BiVO_4$ photoanodes were synthesized via a spin-coating technique. The photocurrent density achieved for the dense electrode reached up to 3 mA/cm^2 at 1.23 V vs. RHE, when paired with a Co-Pi OER co-catalyst. Electrochemical impedance spectroscopy (EIS) measurements showed that the charge transfer kinetics process in this dense $BiVO_4$ was 3-fold faster than in the porous film. The porous film was found to have a higher resistance to charge transfer across the electrode–electrolyte interface, which caused the electrons to accumulate in the CB, and then to eventually recombine with the holes in the VB. However, the authors stated that defective states, induced by the synthesis procedure, may have caused the higher charge recombination in this particular porous photoanode. Indeed, the synthesis of porous $BiVO_4$ via another physical deposition technique, that is, double magnetron sputtering, yielded a photocurrent density of 1.2 mA/cm^2 at 1.23 V vs. RHE [61], which is 4-fold greater than the above mentioned bare $BiVO_4$ that was produced via spin-coating. Besides, similar or better results have recently been obtained by the electrodeposition technique, as described above.

In short, the different characteristics that can be induced by synthesis processes have been identified as being essential to achieve a high performance on bare $BiVO_4$ [60]. The crystallite size was found to have a direct correlation to the O_2 production activity of $BiVO_4$ samples [62] (i.e., doubling the size of the $BiVO_4$ crystals, from 90 to 170 nm increased the rate of O_2 evolution in 5-fold). The preferential orientation towards the {040} facets with respect to the {110} exposed surfaces, is known to have a positive influence on the water oxidation photoactivity of scheelite monoclinic $BiVO_4$ [63]. Moreover, the higher the distortion of the VO_4^{3-} tetrahedron and the lower the V–O distance, the higher is the mobility of the charge carriers in the material, and therefore the more the charge recombination is limited. Finally, a reduced concentration of defects at the grain boundaries of crystals sintered together, which can be achieved by controlling the crystallization (i.e., thermal treatment steps) during the synthesis process, is able to diminish the superficial recombination [60,64].

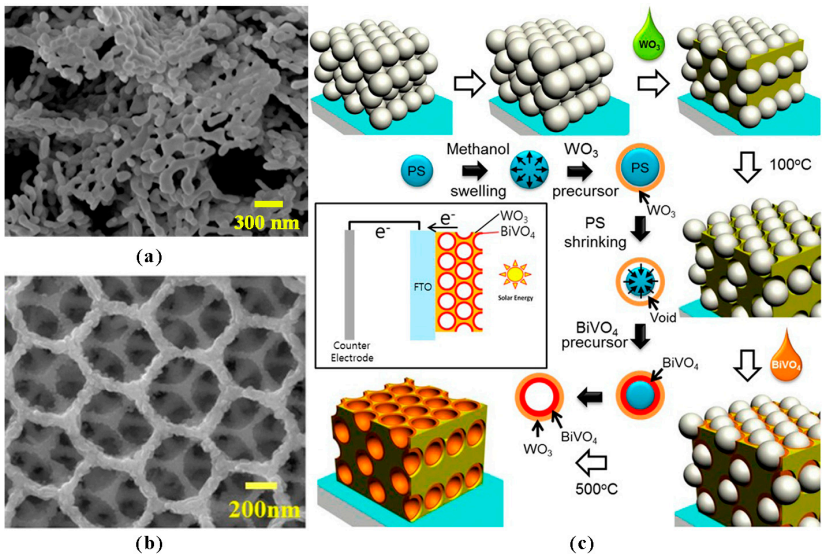

Figure 2. Morphology enhancement techniques for $BiVO_4$ synthesis. (**a**) Field emission scanning electron microscopy (FE-SEM) image of porous $BiVO_4$ on FTO that the authors synthesized using the electrodeposition route suggested by Kim & Choi [43]. (**b**) SEM image and (**c**) schematic diagram of the synthesis of double-deck inverse opal $WO_3/BiVO_4$ synthesized by Ma et al., adapted with permission from [65], Copyright American Chemical Society, 2014.

Effect of Ordered Structures/Inverse Opals

Another method of altering the $BiVO_4$ morphology involves the fabrication of compact, ordered structures, such as inverse opals, which provide an ordered transport path for the electrons, thereby enhancing electron mobility. In order to prepare inverse opals, well-ordered polystyrene (PS) spheres, arranged in crystal templates, are placed on the substrates and are infiltrated with the $BiVO_4$ precursor solution. The PS templates are then removed by annealing, and this leads to the production of inverse opal structured-catalysts. Zhou et al. [35] were able to produce bare $BiVO_4$, with a photocurrent density of 0.6 mA/cm^2 at 1.23 V vs. RHE, using this technique. Doping with 2 at.% Mo increased the photocurrent density to 1.1 mA/cm^2 at 1.23 V vs. RHE.

Ma et al. [65], produced a double-deck heterojunction structure of WO_3 and $BiVO_4$ with an inverse opal nanostructure, which yielded a high photocurrent density of 3.3 mA/cm^2 at 1.23 V vs. RHE, without the aid of a dopant or an OER co-catalyst. Figure 2b shows the FE-SEM image of this photoanode. It was achieved through the use of monodisperse PS scaffold films that had been swollen via a methanol solvent and infiltrated with a WO_3 precursor solution, as shown in Figure 2c. The authors were able to induce the growth of $BiVO_4$ in a controlled manner, thus resulting in its even distribution over the WO_3 skeleton.

2.2.2. Addition of *n*-Type Conductivity Dopants

Doping $BiVO_4$ with Mo and W has been performed extensively [66–74]. Since W and Mo are characterized to be shallow electron donors, their primary effect is to increase the charge carrier density, thereby increasing the electron mobility by increasing the n-type conductivity of the $BiVO_4$ [75]. This, and the superior n-type conductivity induced by Mo doping than by W doping, which results in a higher promoting effect of the former, has been demonstrated by means of first-principle density functional theory (DFT) calculations [67] and experimental results [22,69].

On the other hand, Thalluri et al. [62] identified the important role of the superficial amounts of W and Mo dopants for the water oxidation reaction. They determined that charge carriers separation is enhanced on the surface of $BiVO_4$ for up to a certain amount of such dopants: 0.9 at.% of W or

1.2 at.% of Mo, for which the superficial electron-hole recombination is reduced, and in turn, the $BiVO_4$ photocatalytic activity is improved.

In a study by Pattengale et al. [76], it was reported that the W dopant replaces the V site, causing the bulk structure to change to a mixture of monoclinic and tetragonal scheelite $BiVO_4$ structures, while rendering the Bi centre less distorted than the undoped $BiVO_4$. These structural changes have been inferred to eliminate hole traps, and therefore to extend the electron lifetime.

Park et al. [42] reported that 3 at.% Mo doping on the V site almost doubled the absorbed photon-to-current efficiency (APCE), and also significantly enhanced the photocurrent density of bare $BiVO_4$, from between 0.1 and 0.2 mA/cm^2 at 1.23 V vs. RHE, reaching a final photocurrent density of up to 1.0 mA/cm^2 at 1.23 V vs. RHE. After addition of an FeOOH OER co-catalyst, the photocurrent density increased even more to 3 mA/cm^2 at 1.23 V vs. RHE.

Abdi et al. [48] employed a gradient-doping technique on $BiVO_4$ using 0%–1% of W. This technique has been reported to enhance the charge separation by 1.6-fold. The improvement is due to the induced band bending, which brings about a desirable built-in electric field. The photocurrent density of gradient-doped W reached 1.1 mA/cm^2 at 1.23 V vs. RHE. Adding a Co-Pi OER co-catalyst was found to further enhance the photocurrent density to 3.6 mA/cm^2 at 1.23 V vs. RHE.

Gong et al. [77] reported an increase of up to 2.6-fold in photocurrent density when they performed 10 at.% doping of Mo on bare 150 nm thick $BiVO_4$ that had been produced by magnetron co-sputtering, and reached a photocurrent density of 1.2 mA/cm^2 at 1.23 V vs. RHE.

Doping with PO_4 oxoanion, which increased the activity 30-fold, due to the improved charge transfer in the semiconductor-electrolyte interface, as shown by EIS analyses, has been reported by Won Jun Jo et al. [69].

Tae Woo Kim et al. [28] recently performed N-doping on nanoporous $BiVO_4$ and, in the presence of the FeOOH/NiOOH OEC, they were able to reach a high photocurrent density value of 5 mA/cm^2 at 1.23 V vs. RHE versus the 4 mA/cm^2 at 1.23 V vs. RHE obtained without N-doping. IPCE values were 50% and 60% at 400 and 470 nm, respectively, at 0.6 V vs. RHE. Nitrogen was found to improve both the light absorption and charge transport, due to a further lowering of the band gap energy, which gives access to a wider range of the solar spectrum. This was accomplished by elevating the valence band maximum (VBM), decreasing the static dielectric constant and improving electron mobility.

Jin Hyun Kim et al. [55] produced a dual-doped $BiVO_4$ photoanode, by means of an H-treatment and the use of 3 at.% Mo, which yielded a photocurrent density of about 3 mA/cm^2 at 1.23 V vs. RHE. The H_2 treatment and Mo-doping increased the charge carrier density significantly by two orders of magnitude, due to the formation of intrinsic and extrinsic defects. Doping also extended the diffusion length of the holes. The addition of a Co-Ci OER co-catalyst further increased the photocurrent density to 4.9 mA/cm^2 at 1.23 V vs. RHE.

Monfort et al. [78] used Nb to enhance the photoelectrochemical performance of $BiVO_4$. After the addition of 10 at.% of Nb, the photocurrent density was increased from about 0.5 mA/cm^2 at 1.23 V vs. RHE to about 2 mA/cm^2 at 1.23 V vs. RHE in a $NaHCO_3$ electrolyte. The enhanced activity was attributed to the resulting hierarchical nanostructure, which favoured charge separation.

2.2.3. Heterojunction Formation

The charge recombination in $BiVO_4$ can be attributed to the short carrier diffusion length of approximately 70–100 nm [36], which is much less than the required thickness for sufficient light absorption. A heterojunction [79–81], formed with a more conductive core material, was investigated to address this issue.

In a previously mentioned study by Ma et al. (Figure 2b,c), WO_3 inverse opals were used as the core structure and were reported to have better electron transporting properties than the $BiVO_4$ shell, yielding a photocurrent density of 3.3 mA/cm^2 at 1.23 V vs. RHE. Similarly, a conducting inverse opal network, made of Al-doped ZnO, was used by Zhang et al. [82] as an electron collector, and it yielded a photocurrent density of 1.5 mA/cm^2 at 1.23 V vs. RHE.

Pilli et al. [83] fabricated a $CuWO_4/BiVO_4$ heterojunction by means of electrodeposition of the $CuWO_4$ on FTO and the spray deposition of a highly porous $BiVO_4$ film on the electrodeposited surface. An improvement of up to 1.8-fold in the photocurrent density, which reached values of about 1.6 mA/cm^2 and IPCE of 42% at 420 nm measured at 1.23 V vs. RHE, was attributed to the enhanced charge collection efficiency. This heterojunction caused a shift in the onset potential of up to 0.23 V, when a $NaHCO_3$ electrolyte was used.

A core-shell $WO_3/BiVO_4$ helix nanostructure, synthesized by Shi et al. [44], which was doped with Mo and naturally doped with W from the WO_3 core, produced a photocurrent density of 3.6 mA/cm^2 at 1.23 V vs. RHE. The addition of an FeOOH/NiOOH co-catalyst yielded a high photocurrent density of 5.35 mA/cm^2, and an IPCE of 90% between 330 and 450 nm at 1.23 V vs. RHE. Shi et al. stated that the nanohelix structure improved light absorption, because of the resulting light scattering, and also promoted charge separation by introducing a complex distribution of the electric field.

In a different work, Shi et al. [45] synthesized a mesoporous WO_3 bottom layer that was spin-coated with a Mo-doped $BiVO_4$. Natural doping of the W on the WO_3 layer occurred at the $BiVO_4$, due to their intimate contact during the annealing process. The photocurrent density that was obtained was about 3 mA/cm^2 at 1.23 V vs. RHE, while a further addition of the FeOOH/NiOOH OER co-catalyst brought the photocurrent density to a value of 4 mA/cm^2 at 1.23 V vs. RHE.

Rao et al. [84] fabricated a $WO_3/BiVO_4$ core-shell nanowire photoanode, which was synthesized via a combination of flame vapour deposition and drop-casting methods. A photocurrent density of 3.1 mA/cm^2 at 1.23 V vs. RHE was reached. The W:$BiVO_4$ shell that they synthesized was only 60 nm thick, which is less than the 70–100 nm hole diffusion length reported in literature, as mentioned earlier. In this case, hole/electron charges separation was enhanced because the holes were readily able to reach the semiconductor/electrolyte interface. Furthermore, they reported that the axial electron conductivity of the WO_3 nanowire core was higher than that of the $BiVO_4$ film, thus, the preferential flow of the photogenerated electrons was radially inward to the WO_3 cores.

The highest photocurrent density recorded to date is for the CoPi-coated $WO_3/BiVO_4$ core-shell nanorods shown in Figure 3, synthesized by Pihosh et al. [38], which yielded a photocurrent density of 6.72 mA/cm^2 at 1.23 V vs. RHE, that is, about 90% of the maximum theoretical photocurrent density of $BiVO_4$. An IPCE of 80%–90% was achieved at 400–500 nm at 1 V vs. RHE. The WO_3 nanorods were grown using GLAD, the $BiVO_4$ was synthesized via electrodeposition and the Co-Pi OEC was added via a photo-assisted electrodeposition technique. The key improvement in $BiVO_4$ performance has been attributed to the use of an extremely thin absorber (ETA) heterojunction structure to address the problem concerning the short carrier diffusion length. This minimizes the electron-hole recombination. In addition, Pihosh et al. reported that the ETA structure also enhanced the photon absorption, because of a more efficient light scattering.

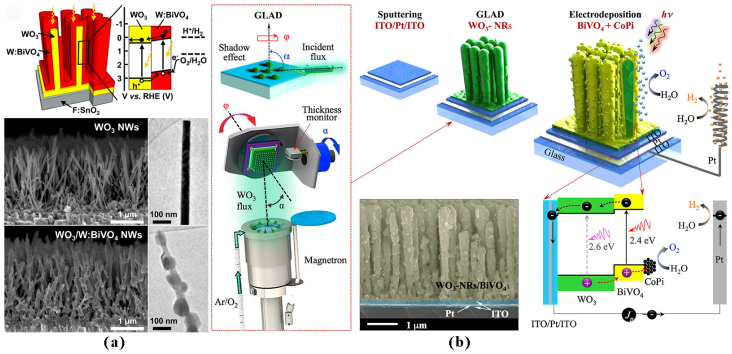

Figure 3. (**a**) $WO_3/BiVO_4$ core-shell nanowires (NWs) according to Rao et al. [84] and (**b**) $WO_3/BiVO_4$ core-shell nanorods (NRs) by Pihosh et al. [38]. Image (**a**) reprinted with permission from [84], Copyright American Chemical Society, 2014. Image (**b**) used under the Creative Commons CC-BY license attributed to [38]. Copyright Nature Publishing Group, 2015.

2.2.4. Use of Passivation Layers

Recent studies on improving the efficiency of semiconductor-based solar water-splitting devices, such as in the review work by Liu et al. [85], introduced surface passivation layers on photoanodes. Passivation layers have been used as an effective strategy to improve the charge-separation and transfer processes across semiconductor–liquid interfaces, and thereby increasing the overall solar energy conversion efficiencies. The passivation effects introduced by these thin layers include a reduction in the charge recombination at surface states, an increase in the reaction kinetics, and the protection of the semiconductor from chemical corrosion (see Figure 4). All of these effects will play a crucial role in achieving highly efficient water-splitting devices in the near future. Semiconductor oxides (i.e., TiO_2, ZnO, $ZnFe_2O_4$, Al_2O_3, Ga_2O_3, In_2O_3), oxygen evolution catalysts (OEC, i.e., CoO_x, Ni, Co-Pi, IrO_x, Pt/SiO_2, Ru/Pt), and other conductive materials such as graphene, have been used as passivation layers on photo-electrodes for water oxidation purposes. The normal thickness of passivation layers is <100 nm, but often only 1–2 nm is adopted to allow charge transfer, by means of tunnelling, when valence band alignment is unfavourable for direct hole conduction. Passivation layers have been fabricated by means of several techniques (i.e. ALD, spin-coating, electrochemical deposition, sputtering, electron beam evaporation, floating transfer or dip-casting).

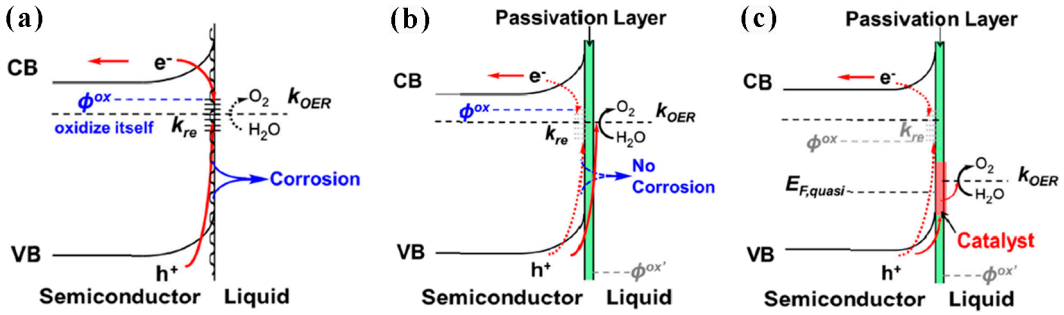

Figure 4. (**a**,**b**) Comparison of an n-type semiconductor photoelectrode with/without a stabilizing passivation layer and with/without corrosion in contact with an aqueous electrolyte. Corrosion may reduce the light absorption and/or generate more surface defect states, which results in a more positive onset potential and a reduced photocurrent; (**c**) Schematic illustration of the band structure of a surface passivation layer on an n-type semiconductor. The photogenerated holes near the surface are in competition with the trap site induced recombination of majority-carriers (e^-) and the charge transfer to the surface layer. The surface recombination rate (k_{re}) and electrode corrosion are suppressed on the passivation surface and the interfacial charge-transfer rate for water oxidation (k_{OER}) is improved. Reproduced and adapted with permission of from [85]. Copyright The Royal Society of Chemistry, 2014.

$BiVO_4$ photoanodes have mainly been investigated in neutral conditions, because $BiVO_4$ gradually dissolves under extreme pH conditions. In order to overcome such a problem, some specific passivation layers were used on this material. Eisenberg et al. [86] used an anodic electrodeposition method to place a thin layer of amorphous TiO_2 (80–120 nm thick deposited for 15–30 s). The prepared film, which is shown in Figure 5, resulted in a significant photocurrent enhancement (up to 5.5-fold) as well as a shift in the photocurrent onset potential to the negative direction of about 0.5 V. The authors explained that the enhancement was in part due to the TiO_2 layer passivating the FTO surface, which was still not completely covered by the W-doped $BiVO_4$. This minimized the back-reduction of the photo-oxidized intermediates on the conducting substrate. The TiO_2 layer also acts passivating defect sites on the surface of the W-doped $BiVO_4$ films, which can serve as recombination centres. The authors also noted that another possible contribution might be an improved charge collection, caused by band bending at the TiO_2–$BiVO_4$ interface.

Ultrathin dual layers of TiO_2 and Ni have also been used to stabilize polycrystalline $BiVO_4$ photoanodes against photocorrosion in an aqueous alkaline (pH = 13) electrolyte [87]. Conformal,

amorphous TiO_2 layers were deposited onto thin $BiVO_4$ films by means of atomic-layer deposition, with Ni being deposited onto the TiO_2 by means of sputtering. Under simulated AM 1.5 illumination, the dual-layer coating extended the lifetime of the $BiVO_4$ photoanodes during photoelectrochemical water oxidation from minutes, for the bare $BiVO_4$, to hours, for the modified electrodes.

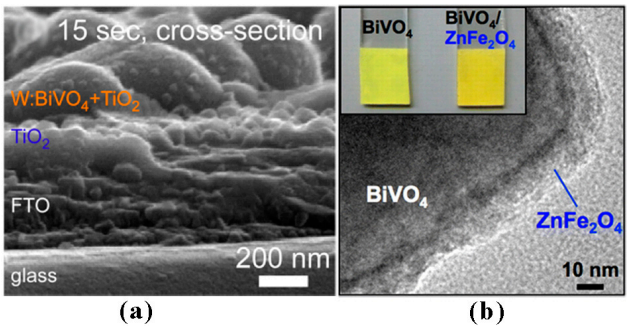

Figure 5. Passivation layers in $BiVO_4$ photoanodes: (**a**) thin amorphous TiO_2, reprinted with permission from [86]. Copyright American Chemical Society, 2014; (**b**) $ZnFe_2O_4$, reprinted with permission from [88]. Copyright American Chemical Society, 2016.

$ZnFe_2O_4$ has also been used as a protection layer to stabilize $BiVO_4$ in a 0.1 M KOH solution [88]. A 10–15 nm thick $ZnFe_2O_4$ layer was conformally placed onto a nanoporous $BiVO_4$ electrode through the photo-depositing of an FeOOH layer, followed by the drop casting of a zinc nitrate solution and annealing. The resulting $BiVO_4/ZnFe_2O_4$ electrode generated a photocurrent density that was >2 mA/cm^2 at 1.23 V versus RHE, with a significantly improved stability, compared to the pristine $BiVO_4$ electrode. The incident and absorbed photon-to-current conversion efficiencies, along with the absorption spectra, suggested that the $ZnFe_2O_4$ protection layer could also contribute to photocurrent generation by increasing photon absorption and electron–hole separation.

It is worth noting that, although significant advantages are possible with a surface passivation layer, other problems may arise. The surface layer creates new interfaces that need to be considered. While a surface layer can improve one property, it may simultaneously make another property worse. However, the engineering of multiple component passivation layers can provide a solution for the many material problems encountered in PEC water splitting.

2.2.5. Substrate Modification

Since the performance of the $BiVO_4$ photoanode is hindered to a great extent by the short hole diffusion length, which is a very evident phenomenon when dealing with flat substrates, efforts have been made to alter the conductive substrate surface by 3D nano-structuring to compensate for this limitation. A few studies have recently reported the 3D structuration of the conductive substrate of the $BiVO_4$ photoanode. However, it should be noted that expensive materials, such as Au and Pt, were used in these techniques to enhance the conductivity of the engineered substrates.

Zhao et al. [89], for instance, deposited the $BiVO_4$ onto textured polydimethylsiloxane (PDMS) substrates fabricated via a water-assisted transfer printing method. This was done to take advantage of the enhanced light absorption, via a dual light-trapping strategy, and of the enhanced surface reactions due to surface roughness. An Au film was deposited onto the SiO_2/Si wafer, via electron beam deposition, to serve as an electron back collector and light reflector. Thin SnO_2 and $BiVO_4$ films were then spin-coated onto this surface. A pristine 80 nm thick $BiVO_4$ photoanode was synthesized, and it exhibited a photocurrent density of 1.37 mA/cm^2, which increased to approximately 2 mA/cm^2 at 1.23 V vs. RHE when enhanced by an FeOOH OER co-catalyst.

Another example concerns the work of Qiu et al. [90], who reported the synthesis of $BiVO_4$ photoanode on an engineered nanocone substrate, which is shown in Figure 6. Engineered substrate

structures, such as the nanocone, offers the advantage of depositing thicker materials with more efficient charge separation. The cone nanostructure was prepared by means of reactive-ion etching of SiO_2, while its conductivity was enhanced through magnetron sputtering of Pt. A SnO_2 film was then applied, by means of ultrasonic spray pyrolysis, as a blocking layer, to reduce back e^- recombination. Finally, $BiVO_4$ was formed via a sol-gel process, and the resulting photocurrent density was 4.18 mA/cm^2 at 1.23 V vs. RHE.

It is worth mentioning that the substrate modification strategy is a key element for the implementation of the photoanodes in a real PEC water splitting device. The development of transparent, conductive, porous, and robust substrates, to be used as supports for photocatalytic electro-active materials, is a demanding, technological development topic. In this context, tin oxide, doped with Sb, In or F, and with nano-crystalline and microporous structures, has recently been developed on glass substrates [91]. However, this kind of substrate can only be employed in PEC devices without separated anode and cathode chambers; otherwise, they can be used as a PEC electrolyzer window that supports a retro-illuminated anodic photocatalyst.

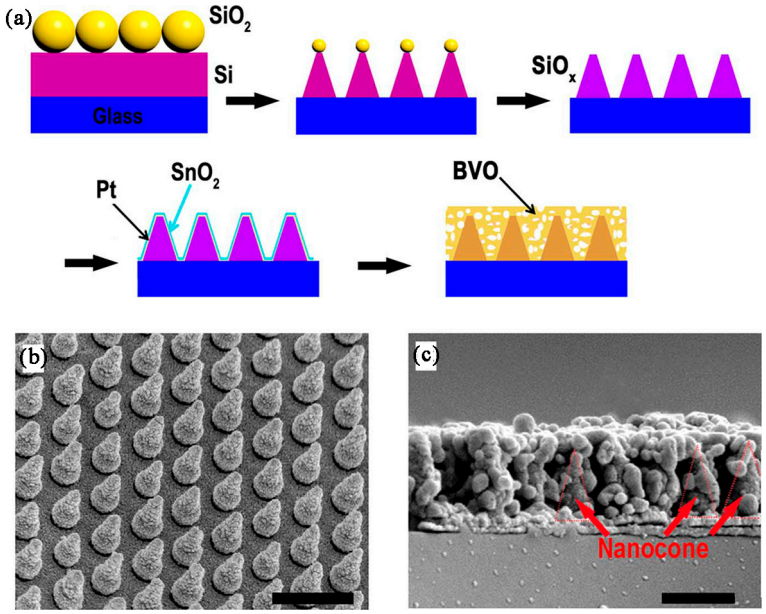

Figure 6. $Pt/SnO_2/Mo:BiVO_4$ on an engineered nanocone substrate. (**a**) Schematic illustration of the fabrication process of the conductive nanocone substrate; (**b**) scanning electron microscope (SEM) image (60° tilting) of the final $SiO_x/Pt/SnO_2$ nanocone arrays; (**c**) cross-sectional SEM images of $Mo:BiVO_4$ on the $SiO_x/Pt/SnO_2$ nanocone substrate. Some exposed nanocones were also marked in the figure (**c**). Scale bars, 500 nm. Images adapted and used under Creative Commons CC-BY-NC license, attributed to [90]. Reprinted with permission of from [90]. Copyright American Association for the Advancement of Science, 2016.

In order for these materials to be used in a Polymeric Exchange Membrane (PEM)-type photo-electrolysis device, to make a membrane-electrode assembly (MEA), the presence of macroporosity is indispensable to allow the diffusion of the water, protons (H^+) and produced gases. For such a purpose, porous metal substrates (i.e., Ni or Ti meshes or foams) have been used as supports for water splitting photocatalysts [92]. Nevertheless, under highly oxidizing conditions, or in the presence of concentrated (acid or basic) electrolytes, they can suffer from low corrosion stability; moreover, they can have a lower surface area than the nanostructured substrates. In order to overcome some of such issues, a new design of FTO-covered quartz laser drilled electrodes was recently proposed by Hernández et al. [93,94]. As shown in Figure 7, this substrate combines several advantages: good transparency (~62% of transmittance), high diffuse reflectance (~37%), low electric

resistance, ($\leq$40 Ω/square), and easy adhesion of the photo-catalysts; in addition, this substrate allows the permeation of water, protons and gases, due to the presence of micrometric conical holes (~30–150 μm).

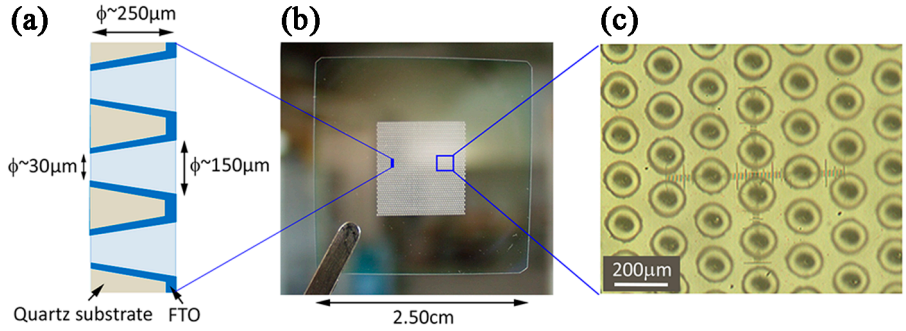

Figure 7. The FTO-laser-drilled electrode: (**a**) scheme of the cross-section; (**b**) photograph and (**c**) optical microscopy image (view from FTO side). Reprinted with permission from [94]. Copyright Elsevier, 2014.

2.3. Summary of $BiVO_4$-Based Photoanodes with Photocurrent Densities > 3.5 mA/cm^2 at 1.23 V vs. RHE

A summary of the $BiVO_4$-based photoanodes that have higher photocurrent densities than 3.5 mA/cm^2 at 1.23 V vs. RHE is shown in Table 1, along with their measured efficiencies and synthesis methods. These are currently the top-performing $BiVO_4$ photoanodes in the literature.

Table 1. $BiVO_4$-based photoanodes with the highest photocurrent density to date.

Photoanode	Photocurrent Density [1] (mA/cm^2)	Illuminated Area (cm^2)	Efficiency	Stability	Ref.
WO_3/$BiVO_4$ nanorods with Co-Pi	6.72	Unspecified. Electrode Area: 0.226	IPCE 80%–90%, 400–500 nm at 1 V vs. RHE	Not reported	[38]
SiO_x/Pt/SnO_2 Mo:$BiVO_4$ nanocone with Fe(Ni)OOH	5.82	0.25	IPCE > 75%, <460 nm, at 1.23 V vs. RHE; APBE ~2.05% at 0.62 V vs. RHE	About 5.8 mA/cm^2 at 1.23 V vs. RHE for 5 h	[90]
WO_3/(W, Mo):$BiVO_4$ helix nanostructures with FeOOH/NiOOH	5.35	Unspecified. Electrode Area: 2.25	IPCE 90%, 330–450 nm at 1.23 V vs. RHE	About 3 mA/cm^2 at 1.23 V vs. RHE for 7 days (8.7% decay)	[44]
N:$BiVO_4$ with FeOOH/NiOOH	5.0	0.1–0.2	IPCE 50%–60%, 400–470 nm at 0.6 V vs. RHE	About 3.2 mA/cm^2 at 0.6 V vs. RHE for 30 h	[28]
(H, 3% Mo):$BiVO_4$ with Co-Ci	4.9	Unspecified	IPCE ~80%, 420 nm at 1.23 V vs. RHE	About 3.5 mA/cm^2 at 1.03 V vs. RHE for 12 h	[55]
Nanoporous $BiVO_4$ with FeOOH/NiOOH	4.2	0.2	APBE 2.2% at 0.58 V vs. CE (Pt)	2.73 mA/cm^2 at 0.6 V vs. RHE for 48 h	[43]
SiO_x/Pt/SnO_2 Mo:$BiVO_4$ nanocone	4.18	0.25	ABPE about 0.75% at 0.87 V vs. RHE	Not reported	[90]
WO_3/(W, Mo):$BiVO_4$ with FeOOH/NiOOH	4.0	Unspecified. Electrode area: 2.25	Not reported	Not reported	[45]
W(0%–1%) gradient-doped $BiVO_4$ with Co-Pi	3.6	Unspecified	Carrier separation efficiency of up to 80%	Not reported	[48]
Nanoporous $BiVO_4$ with FeOOH	3.6	0.2	Not reported	Not reported	[43]

[1] Measured for a 3-electrode system at 1.2–123 V vs. RHE, AM 1.5 G illumination and intensity of 1 sun (100 mW/cm^2).

It can be seen from Table 1 that the best-performing $BiVO_4$ photoanodes to-date are generally composed of the following components: (1) a heterojunction with conductive WO_3 as the core structure, which is synthesized via physical deposition techniques, such as glancing and oblique angle deposition;

(2) a $BiVO_4$ shell structure synthesized via a solution-based technique, with a notable preference for scalable electrodeposition methods; (3) dopants, usually Mo and W, which increase the charge carrier density and are normally introduced with the $BiVO_4$ precursors in a solution; and (4) OER co-catalysts, which are generally Co-Pi or FeOOH/NiOOH that are used for the enhancement of the water oxidation kinetics and incorporated via a photo-assisted electrodeposition technique.

3. Critical Issues Hampering the Scale-Up of $BiVO_4$-Based PECs

While there have been numerous efforts to study the fundamental aspects of a PEC water splitting system, and in particular, the critical photoanode assembly, the road to building efficient, robust, and scalable functional devices still seems long and challenging. The target is to reach at least 10% Solar-to-Hydrogen (STH) efficiency, and a lifetime of 10 years, for a device that costs US\$100/m^2 to manufacture, before these devices can be competitive with the PV + electrolyzer system [95]. However, even putting together the best individual components cannot guarantee the formation of the most efficient device. It is necessary for those components to work in conditions in which they are compatible. This, however, is largely dictated by the interplay of certain factors, such as the operating conditions and the material properties, which in turn are dictated by the adopted synthesis methods, stability, scalability, and costs.

3.1. Synthesis Scalability

As can be seen from Table 1, the top performing $BiVO_4$-based photoanodes prepared up till now have a maximum deposited and illuminated area of 2.5 cm^2, although in some cases this area has not been specified. Nevertheless, it is known that the significant material properties that can affect the photoelectrochemical activity are influenced to a great extent, if not dictated, by the adopted synthesis method and the size of the electrode. As pointed out by Hernández et al. [60], the non-uniformity of a $BiVO_4$ film surface leads to issues in the preparation of larger-sized electrodes, which is necessary for practical applications at a larger scale. The spin-coating technique has not yielded a uniform surface for electrodes as large as 6 cm^2, and the testing of these electrodes at different illuminated areas yielded different results. Illuminating a 6 cm^2 area versus a 1 cm^2 area halved the photocurrent density. Thus, emphasis should be on the use of scalable techniques, i.e., those that are able to produce uniform and efficient electrodes with large deposited areas.

Synthesizing $BiVO_4$ photoanodes with high transparency is also essential for their use as light absorbers in tandem cell devices [45]. Thus, the thickness of the material deposited onto the substrate should be controlled and limited according to the chosen synthesis technique.

Moreover, the costs associated with the synthesis procedure should be considered in the scaling up of PEC water splitting operations. Not only are these dependent on the cost of raw materials, but also on the manner and the procedure by which the synthesis is conducted and on the techniques employed to do so. This necessitates the use of less-complicated steps and mild operating conditions in order to strike a balance between efficiency and cost-effectiveness. For example, electrodeposition, which is a solutions-based synthesis technique, could prove to be very viable in this context. It is an already proven industrial process, as it is used in industrial car painting, and it offers fine-tuning opportunities for the morphology and other synthesis parameters due to its solutions-based nature [11]. In the same manner, some physical deposition techniques such as the co-sputtering method are currently used at high scales for the deposition of thin films for electronic components.

3.2. Oxygen Evolution Catalysts

Among the most successful and most efficient OECs known to date, and which are able to operate under almost neutral pH conditions, the use of the Co-Pi type catalyst can be considered an easily scalable solution. Self-healing catalysts, such as Co-Pi, Co-Ci, and Co-Bi, can be deposited in situ with a certain amount (e.g. 0.5 mM) of Co^{2+} ions in a solution of phosphate, carbonate, and borate buffers, respectively, through the application of a fixed potential. However, the use of these catalysts

requires the adoption of a buffered electrolyte for the control of the pH in the anodic chamber as well as a proper control of the amount of Co^{2+} ions in the solution. The latter aspect is indispensable to guarantee the self-healing property of the electrode; however, it can also cause an overloading of Co-Pi type catalysts on the surface of the electrode, which can happen when either the Co^{2+} in the solution or the applied bias are too high, with a consequent deactivation of the photoelectrode. In fact, the Co-Pi photo-electrodeposition at 1.32 V vs. RHE over a period of 60 s has been reported to be the optimum conditions for an enhanced performance of $BiVO_4$ photoanodes, while longer times can lead to a reduction in the photo-electrode activity [59]. Therefore, long-term stability and deactivation issues still have to be resolved before the current Co-based OECs can be used at a large scale.

The development of non-noble metal OECs that operate in acidic conditions is of utmost importance. If the PEC water splitting device is to be operated using pure water, as is the case of PEM electrolyzers, the anodic chamber is bound to become acidic, due to the induced H^+ gradient in the cell, since H^+ ions continuously form in the anode and migrate towards the cathode. At present, this issue still remains a challenge, as only noble-metal (Ru and Ir) -based OECs are able to dominate acidic media stability [56,57]. This is particularly challenging for the use of OECs with $BiVO_4$-based photoanodes, because $BiVO_4$ gradually dissolves when subjected to a solution with extreme pH conditions. Hence, a proper engineering of the interphases between the $BiVO_4$, a passivating/protecting layer, and the OEC is required to sustain a stable operation.

In addition, in order to be used in integrated devices, the OECs have to be transparent enough to avoid blocking the light as it passes through the light-absorbing photoanode in a tandem illumination mode. However, when made of non-noble metal oxides, relatively higher catalyst loadings are needed to achieve a comparable performance with that of noble metals. The higher catalyst loading affects the transparency of the material and may induce the eventual optical losses due to absorption and light scattering [96].

3.3. Long-Term Stability

In order to be practical, PEC water splitting systems have to be stable for a long period of time, the typical benchmark being a lifetime of 10 years [97,98]. However, achieving such a lifetime still remains a challenge as scientists are still trying to overcome the effect of the strong reductive and oxidative properties of the photogenerated electron-hole pair on the stability of semiconductor electrodes.

Toma et al. [99] recently performed a mechanistic study on the chemical and photochemical transformations of $BiVO_4$ photoanodes in which insights are given about issues concerning the source of instability in $BiVO_4$ photoanodes. In this study, it was shown that the degradation of the $BiVO_4$ photoanodes takes place under all aqueous testing conditions and was seen to be accelerated by illumination, as well as by increase of the pH and of the applied anodic bias. This phenomenon was prevalently attributed to the following: (1) an inability to achieve self-passivation, brought about by the inability to form a stable Bi-O surface phase, due to kinetic limitations on the room-temperature structural transformation of V-deprived degradation product; and (2) an accumulation of holes on the surface of the lattice, which were observed to cause the $BiVO_4$ destabilization.

Among the top-performing $BiVO_4$-based photoanodes summarized in Table 1, the longest stability test was for the WO_3/(W, Mo):$BiVO_4$ helix nanostructures with FeOOH/NiOOH [44], which lasted seven days, and demonstrated a decay of 8.7% in the photocurrent density. Evidently, the 10-year stability target is still far from being achieved as current research trends are still focusing on solving the problem of inefficiency.

3.4. Large-Scale PEC Prototype Issues: The ARTIPHYCTION Experience

To the best of the authors' knowledge, the partners in the EU-FP7 FCH JU founded project: ARTIPHYCTION (No. 303435) were the first to develop a large-scale 1.6 m^2 PEC that was validated in TRL5 (see Figure 8), for the direct production of H_2 from sunlight via water splitting [100]. The best

results were obtained with a CoPi-catalysed Mo-doped $BiVO_4$ photoanode (made by means of a spin-coating method) and the Co nanoparticle-based cathodic electro-catalyst that was used in the final Artiphyction prototype, which showed a potential of a 3% overall sunlight conversion efficiency into H_2. However, mass-transfer and kinetics limitation phenomena (bubbles formation and accumulation on the electrode surface) caused a decrease in the performance of up to about 2% during long-term operation.

The significant problem of bubble formation and evolution on a $BiVO_4$ photoanode, and their consequences on the efficiency of a photoelectrochemical cell were recently analysed through theoretical models in the framework of the same project [100,101]. Hernández et al. [102] proposed a percolation approach to explain the time variation (decrease) of the photocurrent density during bubble generation in a porous $BiVO_4$ photoanode. They proposed a correlation between a bubble-covering factor (β) and the current density, for different applied bias and illumination conditions. In fact, the produced O_2 bubbles first tend to stick to the electrode surface, thus decreasing the effective area, increasing the interfacial electric resistance, and increasing the ohmic losses. In addition, Gliozzi et al. [101] developed a model based on the adsorption theory (similar to Langmuir's isotherm). They showed that the time dependence of the current density is influenced by two characteristic periods of time: one short period, related to the electric charging of the surface layer, and another long period, related to the kinetics of the O_2 bubble coverage (adsorption–desorption). Moreover, they showed that the latter also depended on the applied bias potential.

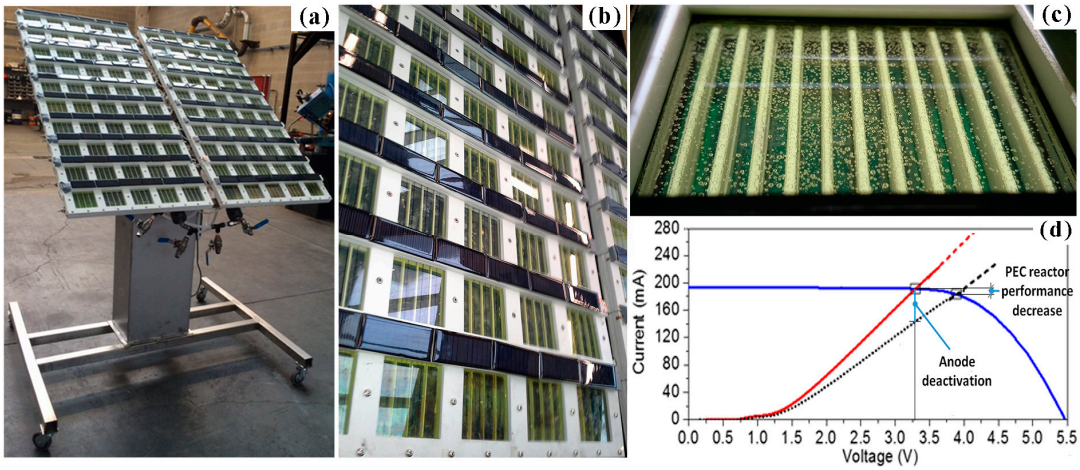

Figure 8. (**a**) Photograph and (**b**) close view of the 1.6 m^2 Artiphyction prototype made of 100 PEC cells (each of them with a 8 × 8 cm^2 $BiVO_4$-based window); (**c**) photo of a single PEC cell of the prototype under operation; (**d**) I–V plots for a single PEC window of the Artiphyction prototype. Blue line: I–V power generation curve of the Si-PV cell for each window; red and black line/dotted line: initial and final PEC cell performance under 1 sun irradiation (AM 1.5 G); light-blue lines: possible performance degradation of a PEC cell prototype.

A unique feature of the Artiphyction system, other than being the first attempt to scale-up a PEC for water splitting, is that the outer case of the photo-electrolyser was exploited to insert low-cost Si PV cells that provide the bias potential necessary for the prototype. In addition, in order to guarantee a continuous operation for the 1000 h of testing, the system was designed so that each single unit of the PEC reactor would operate close to the maximum point in the I–V diagram. Therefore, in the case of system deactivation, such a point should be shifted towards higher voltages, as can be seen in Figure 8d, in order to keep the current drop and the H_2 production rate reduction at less than 10%. Hence, the maximum overall H_2 production of this prototype was slightly higher than 1 g/h.

The previous results indicate that, in order to fully achieve the ambitious goals of STH efficiency (>10%) and a stability of more than 10 years, more engineering efforts are still necessary to improve

the photoelectrolyser reactor design, with the aim of ameliorating its fluid dynamics, as well as of a further optimizing the photo-electroactive materials so as to achieve their efficient scale-up.

3.5. $BiVO_4$-Photoanode PEC Tandem Device Assemblies

Although relatively favourable and strategic, compared to other metal oxides, such as Fe_2O_3 and WO_3, the conduction band edge of $BiVO_4$ still does not allow water to be completely split without an applied bias, thus, its use as a photoanode in tandem PEC water splitting devices has also been studied recently.

The most frequently studied PEC tandem assemblies today are those made with multijunction and perovskite photovoltaic (PV) solar cells. The most notable $BiVO_4$-photoanode PEC tandem devices with PV solar cells reported to date are summarized in Table 2.

Recent developments of $BiVO_4$-photoanode PEC tandem devices have yielded an STH efficiency that reaches up to 8.1%. While this is very encouraging, the challenge remains concerning the costs of fabricating these materials at a larger scale. Multijunction PV cells are complex and expensive, and the current tandem assemblies still cannot compete with the conventional ways of producing H_2 which costs US$ 2–3/kg [103]. Meanwhile, the emerging perovskite solar cells could alternatively offer a cheaper solution. However, more research is required to solve the intrinsic stability issues that still remain for perovskite solar cells.

Table 2. $BiVO_4$ photoanode-based PEC–PV/perovskite Tandem Devices.

$BiVO_4$ Photoanode	In Tandem with	STH Efficiency	Photocurrent Density [1] (mA/cm^2)	Stability	Ref.
$WO_3/BiVO_4$ nanorods with Co-Pi	2-jn GaAs/InGaAsP	8.1%	6.56	Tested for 1 h, sustained for 1 h	[38]
WO_3/(W, Mo):$BiVO_4$ with FeOOH/NiOOH	Hybrid cDBR	7.1%	5.7	Tested for 10 h, sustained for 10 h	[45]
SiOx/Pt/SnO_2 Mo:$BiVO_4$ nanocone with Fe(Ni)OOH	perovskite solar cell	6.2%	5.82	5.8% decay over 10 h	[90]
W(0%–1%) gradient-doped $BiVO_4$ with Co-Pi	2-jn a-Si PV	4.9%	4.0	Tested for 1 h, sustained for 1 h	[48]
(H, 3% Mo):$BiVO_4$ with Co-Ci	$CH_3NH_3PbI_3$ perovskite single jn	Wired: 4%Wireless: 3%	4.8	Tested for 10 h, sustained for 10 h	[55]

[1] Measured at 1.2–123 V vs. RHE, AM 1.5 G illumination and intensity of 1 sun (100 mW/cm^2).

4. Conclusions

PEC water splitting and artificial photosynthesis offer a truly sustainable way of converting solar energy into chemical energy. The use of $BiVO_4$-based photoanodes for PEC systems has improved greatly over the years and continues to improve, as pointed out in this review work, and in time this will lead to the fabrication of a more efficient and scalable device. Certain constraints still have to be addressed in order to put this into practice, e.g., the long-time stability and scale-up of both the photoanode and the PEC device; however, going in this direction and focusing on solving such issues could pave the way to the commercialization of the PEC technology, for a sustainable production of clean fuels and chemicals via the artificial photosynthesis process.

Acknowledgments: The authors would like to acknowledge the EACEA Erasmus + SINCHEM Grant (FPA 2013-0037), the European Commission FP7 Projects: NMP-2012 Eco^2CO_2 (No. 309701), and FCH JU Artiphyction (No. 303435) for the financial support.

Author Contributions: K.R.T. did the literature review; K.R.T. and S.H. equally contributed in writing the paper; N.R. conceived and critically revised the manuscript.

Conflicts of Interest: The authors declare no conflict of interest.

References

1. Gray, H.B. Powering the planet with solar fuel. *Nat. Chem.* **2009**, *1*, 7. [CrossRef] [PubMed]
2. Von de Krol, R.; Grätzel, M. Photoelectrochemical Hydrogen Production. *Electron. Mater. Sci. Technol.* **2012**, *102*, 13–21.
3. Chen, Z.; Dinh, H.N.; Miller, E. Introduction. In *Photoelectrochemical Water Splitting*; Springer: New York, NY, USA, 2013; pp. 1–5. [CrossRef]
4. Walter, M.G.; Warren, E.L.; McKone, J.R.; Boettcher, S.W.; Mi, Q.; Santori, E.A.; Lewis, N.S. Solar Water Splitting Cells. *Chem. Rev.* **2010**, *110*, 6446–6473. [CrossRef] [PubMed]
5. Martinez Suarez, C.; Hernández, S.; Russo, N. $BiVO_4$ as photocatalyst for solar fuels production through water splitting: A short review. *Appl. Catal. A Gen.* **2015**, *504*, 158–170. [CrossRef]
6. Fujishima, A.; Honda, K. Electrochemical photolysis of water at a semiconductor electrode. *Nature* **1972**, *238*, 37–38. [CrossRef] [PubMed]
7. Hurst, J.K. Catalysts for Solar Fuel Production. *Science* **2010**, *328*, 315–316. [CrossRef] [PubMed]
8. Grätzel, M.; Moser, J. Solar Energy Conversion. In *Electron Transfer in Chemistry*; Wiley-VCH: Weiheim, Germany, 2001; Volume 5, pp. 589–644.
9. Betley, T.A.; Wu, Q.; Van Voorhis, T.; Nocera, D.G. Electronic design criteria for O–O bond formation via metal-oxo complexes. *Inorg. Chem.* **2008**, *47*, 1849–1861. [CrossRef] [PubMed]
10. Inoue, H.; Shimada, T.; Kou, Y.; Nabetani, Y.; Masui, D.; Takagi, S.; Tachibana, H. The water oxidation bottleneck in artificial photosynthesis: How can we get through it? An alternative route involving a two-electron process. *ChemSusChem* **2011**, *4*, 173–179. [CrossRef] [PubMed]
11. Kang, D.; Kim, T.W.; Kubota, S.R.; Cardiel, A.C.; Cha, H.G.; Choi, K.S. Electrochemical Synthesis of Photoelectrodes and Catalysts for Use in Solar Water Splitting. *Chem. Rev.* **2015**, *115*, 12839–12887. [CrossRef] [PubMed]
12. Young, K.J.; Martini, L.A.; Milot, R.L.; Snoeberger, R.C.; Batista, V.S.; Schmuttenmaer, C.A.; Crabtree, R.H.; Brudvig, G.W. Light-driven water oxidation for solar fuels. *Coord. Chem. Rev.* **2012**, *256*, 2503–2520. [CrossRef] [PubMed]
13. Tachibana, Y.; Vayssieres, L.; Durrant, J.R. Artificial photosynthesis for solar water-splitting. *Nat. Photonics* **2012**, *6*, 511–518. [CrossRef]
14. Blakemore, J.D.; Crabtree, R.H.; Brudvig, G.W. Molecular Catalysts for Water Oxidation. *Chem. Rev.* **2015**, *115*, 12974–13005. [CrossRef] [PubMed]
15. Harriman, A.; Pickering, I.J.; Thomas, J.M.; Christensen, P.A. Metal Oxides as Heterogeneous Catalysts for Oxygen Evolution under Photochemical Conditions. *J. Chem. Soc. Faraday Trans. 1* **1988**, *84*, 2795–2806. [CrossRef]
16. Kiwi, J.; Grätzel, M. Hydrogen evolution from water induced by visible light mediated by redox catalysis. *Nature* **1979**, *281*, 657–658. [CrossRef]
17. Roth, R.; Waring, J. Synthesis and stability of bismutotantalite, stibiotantalite and chemically similar ABO_4 compounds. *Am. Miner.* **1963**, *18*, 1348–1356.
18. Lim, A.R.; Choh, S.H.; Jang, M.S. Prominent ferroelastic domain walls in $BiVO_4$ crystal. *J. Phys. Condens. Matter* **1995**, *7*, 7309–7323. [CrossRef]
19. Kudo, A.; Omori, K.; Kato, H. A Novel Aqueous Process for Preparation of Crystal Form-Controlled and Highly Crystalline $BiVO_4$ Powder from Layered Vanadates at Room Temperature and Its Photocatalytic and Photophysical Properties. *J. Am. Chem. Soc.* **1999**, *121*, 11459–11467. [CrossRef]
20. Bhattacharya, A.K. Phase transition in $BiVO_4$. *Mater. Lett.* **1997**, *30*, 7–13. [CrossRef]
21. Walsh, A.; Yan, Y.; Huda, M.N.; Al-Jassim, M.M.; Wei, S.-H. Band Edge Electronic Structure of $BiVO_4$: Elucidating the Role of the Bi s and V d orbitals. *Chem. Mater.* **2009**, *21*, 547–551. [CrossRef]
22. Cooper, J.K.; Gul, S.; Toma, F.M.; Chen, L.; Glans, P.-A.; Guo, J.; Ager, J.W.; Yano, J.; Sharp, I.D. Electronic Structure of Monoclinic $BiVO_4$. *Chem. Mater.* **2014**, *26*, 5365–5373. [CrossRef]
23. Kudo, A.; Ueda, K.; Kato, H.; Mikami, I. Photocatalytic O_2 evolution under visible light irradiation on $BiVO_4$ in aqueous $AgNO_3$ solution. *Catal. Lett.* **1998**, *53*, 229–230. [CrossRef]

24. Payne, D.J.; Robinson, M.D.M.; Egdell, R.G.; Walsh, A.; McNulty, J.; Smith, K.E.; Piper, L.F.J. The nature of electron lone pairs in $BiVO_4$. *Appl. Phys. Lett.* **2011**, *98*, 46–49. [CrossRef]
25. Hu, S.; Xiang, C.; Haussener, S.; Berger, A.D.; Lewis, N.S. An analysis of the optimal band gaps of light absorbers in integrated tandem photoelectrochemical water-splitting systems. *Energy Environ. Sci.* **2013**, *6*, 2984–2993. [CrossRef]
26. Abdi, F.F.; Firet, N.; van de Krol, R. Efficient $BiVO_4$ Thin Film Photoanodes Modified with Cobalt Phosphate Catalyst and W-doping. *ChemCatChem* **2013**, *5*, 490–496. [CrossRef]
27. Park, Y.; McDonald, K.J.; Choi, K.S. Progress in bismuth vanadate photoanodes for use in solar water oxidation. *Chem. Soc. Rev.* **2013**, 2321–2337. [CrossRef] [PubMed]
28. Kim, T.W.; Ping, Y.; Galli, G.A.; Choi, K.S. Simultaneous enhancements in photon absorption and charge transport of bismuth vanadate photoanodes for solar water splitting. *Nat. Commun.* **2015**, *6*, 8769. [CrossRef] [PubMed]
29. McDonald, K.J.; Choi, K.S. A new electrochemical synthesis route for a BiOI electrode and its conversion to a highly efficient porous $BiVO_4$ photoanode for solar water oxidation. *Energy Environ. Sci.* **2012**, *5*, 8553–8557. [CrossRef]
30. Taylor, S.R. Abundance of chemical elements in the continental crust: A new table. *Geochim. Cosmochim. Acta* **1964**, *28*, 1273–1285. [CrossRef]
31. Kronawitter, C.X.; Vayssieres, L.; Shen, S.; Guo, L.; Wheeler, D.A.; Zhang, J.Z.; Antoun, B.R.; Mao, S.S. A perspective on solar-driven water splitting with all-oxide hetero-nanostructures. *Energy Environ. Sci.* **2011**, *4*, 3889–3899. [CrossRef]
32. Cho, S.; Jang, J.W.; Lee, K.H.; Lee, J.S. Research update: Strategies for efficient photoelectrochemical water splitting using metal oxide photoanodes. *APL Mater.* **2014**, *2*, 10703. [CrossRef]
33. Ma, Y.; Pendlebury, S.R.; Reynal, A.; le Formal, F.; Durrant, J.R. Dynamics of photogenerated holes in undoped $BiVO_4$ photoanodes for solar water oxidation. *Chem. Sci.* **2014**, *5*, 2964. [CrossRef]
34. Sinclair, T.S.; Hunter, B.M.; Winkler, J.R.; Gray, H.B.; Astrid, M.M. Materials Horizons Factors affecting bismuth vanadate photoelectrochemical performance. *Mater. Horiz.* **2015**, 22–24.
35. Zhou, M.; Bao, J.; Xu, Y.; Zhang, J.; Xie, J.; Guan, M.; Wang, C.; Wen, L.; Lei, Y.; Xie, Y. Photoelectrodes based upon Mo:$BiVO_4$ inverse opals for photoelectrochemical water splitting. *ACS Nano* **2014**, *8*, 7088–7098. [CrossRef] [PubMed]
36. Abdi, F.F.; Savenije, T.J.; May, M.M.; Dam, B.; Van De Krol, R. The Origin of Slow Carrier Transport in $BiVO_4$ Thin Film Photoanodes. *J. Phys. Chem. Lett.* **2013**, *4*, 2752–2757. [CrossRef]
37. Retti, A.J.E.; Lee, H.C.; Marshall, L.G.; Lin, J.-F.; Capan, C.; Lindemuth, J.; McCloy, J.S.; Zhou, J.; Bard, A.J.; Mullins, C.B. Combined Charge Carrier Transport and Photoelectrochemical Characterization of $BiVO_4$ Single Crystals: Intrinsic Behavior of a Complex Metal Oxide. *J. Am. Chem. Soc.* **2013**, *135*, 11389–11396. [CrossRef] [PubMed]
38. Pihosh, Y.; Turkevych, I.; Mawatari, K.; Uemura, J.; Kazoe, Y.; Kosar, S.; Makita, K.; Sugaya, T.; Matsui, T.; Fujita, D.; et al. Photocatalytic generation of hydrogen by core-shell WO_3/$BiVO_4$ nanorods with ultimate water splitting efficiency. *Sci. Rep.* **2015**, *5*, 11141. [CrossRef] [PubMed]
39. Kim, J.H.; Jang, J.W.; Kang, H.J.; Magesh, G.; Kim, J.Y.; Kim, J.H.; Lee, J.; Lee, J.S. Palladium oxide as a novel oxygen evolution catalyst on $BiVO_4$ photoanode for photoelectrochemical water splitting. *J. Catal.* **2014**, *317*, 126–134. [CrossRef]
40. Wang, D.; Li, R.; Zhu, J.; Shi, J.; Han, J.; Zong, X.; Li, C. Photocatalytic water oxidation on $BiVO_4$ with the electrocatalyst as an oxidation cocatalyst: Essential relations between electrocatalyst and photocatalyst. *J. Phys. Chem. C* **2012**, *116*, 5082–5089. [CrossRef]
41. Seabold, J.A.; Choi, K.S. Efficient and stable photo-oxidation of water by a bismuth vanadate photoanode coupled with an iron oxyhydroxide oxygen evolution catalyst. *J. Am. Chem. Soc.* **2012**, *134*, 2186–2192. [CrossRef] [PubMed]
42. Park, Y.; Kang, D.; Choi, K.-S. Marked enhancement in electron-hole separation achieved in the low bias region using electrochemically prepared Mo-doped $BiVO_4$ photoanodes. *Phys. Chem. Chem. Phys.* **2014**, *16*, 1238–1246. [CrossRef] [PubMed]

43. Kim, T.W.; Choi, K.-S. Nanoporous $BiVO_4$ Photoanodes with Dual-Layer Oxygen Evolution Catalysts for Solar Water Splitting. *Science* **2014**, *343*, 990–994. [CrossRef] [PubMed]
44. Shi, X.; Choi, I.Y.; Zhang, K.; Kwon, J.; Kim, D.Y.; Lee, J.K.; Oh, S.H.; Kim, J.K.; Park, J.H. Efficient photoelectrochemical hydrogen production from bismuth vanadate-decorated tungsten trioxide helix nanostructures. *Nat. Commun.* **2014**, *5*, 4775. [CrossRef] [PubMed]
45. Shi, X.; Jeong, H.; Oh, S.J.; Ma, M.; Zhang, K.; Kwon, J.; Choi, I.T.; Choi, I.Y.; Kim, H.K.; Kim, J.K. Unassisted photoelectrochemical water splitting exceeding 7% solar-to-hydrogen conversion efficiency using photon recycling. *Nat. Commun.* **2016**, *7*, 11943. [CrossRef] [PubMed]
46. Kanan, M.W.; Nocera, D.G. In situ formation of an oxygen-evolving catalyst in neutral water containing phosphate and Co^{2+}. *Science* **2008**, *321*, 1072–1075. [CrossRef] [PubMed]
47. Lutterman, D.A.; Surendranath, Y.; Nocera, D.G. A Self-Healing Oxygen-Evolving Catalyst. *J. Am. Chem. Soc.* **2009**, *131*, 3838–3839. [CrossRef] [PubMed]
48. Abdi, F.F.; Han, L.; Smets, A.H.M.; Zeman, M.; Dam, B.; van de Krol, R. Efficient solar water splitting by enhanced charge separation in a bismuth vanadate-silicon tandem photoelectrode. *Nat. Commun.* **2013**, *4*, 1–7. [CrossRef] [PubMed]
49. Zhong, D.K.; Gamelin, D.R. Photoelectrochemical Water Oxidation by Cobalt Catalyst ("Co-Pi")α-Fe_2O_3 Composite Photoanodes Oxygen Evolution and Resolution of a Kinetic Bottleneck. *J. Am. Chem. Soc.* **2010**, *132*, 4202–4207. [CrossRef] [PubMed]
50. Pilli, S.K.; Furtak, T.E.; Brown, L.D.; Deutsch, T.G.; Turner, J.A.; Herring, A.M. Cobalt-phosphate (Co-Pi) catalyst modified Mo-doped $BiVO_4$ photoelectrodes for solar water oxidation. *Energy Environ. Sci.* **2011**, *4*, 5028. [CrossRef]
51. Zhong, D.K.; Choi, S.; Gamelin, D.R. Near-Complete Suppression of Surface Recombination in Solar Photoelectrolysis by "Co-Pi" Catalyst-Modified W:$BiVO_4$. *J. Am. Chem. Soc.* **2011**, *133*, 18370–18377. [CrossRef] [PubMed]
52. Zhong, M.; Hisatomi, T.; Kuang, Y.; Zhao, J.; Liu, M.; Iwase, A.; Jia, Q.; Nishiyama, H.; Minegishi, T.; Nakabayashi, M.; et al. Surface Modification of CoO_x Loaded $BiVO_4$ Photoanodes with Ultrathin *p*-Type NiO Layers for Improved Solar Water Oxidation. *J. Am. Chem. Soc.* **2015**, *137*, 5053–5060. [CrossRef] [PubMed]
53. Joya, K.S.; Takanabe, K.; De Groot, H.J.M. Surface generation of a cobalt-derived water oxidation electrocatalyst developed in a neutral HCO^{3-}/CO_2 system. *Adv. Energy Mater.* **2014**, *4*, 2–7.
54. Kim, J.H.; Magesh, G.; Kang, H.J.; Banu, M.; Kim, J.H.; Lee, J.; Lee, J.S. Carbonate-coordinated cobalt Co-catalyzed $BiVO_4/WO_3$ composite photoanode tailored for CO_2 reduction to fuels. *Nano Energy* **2015**, *15*, 153–163. [CrossRef]
55. Kim, J.H.; Jo, Y.; Kim, J.H.; Jang, J.W.; Kang, H.J.; Lee, Y.H.; Kim, D.S.; Jun, Y.; Lee, J.S. Wireless Solar Water Splitting Device with Robust Cobalt-Catalyzed, and Perovskite Solar Cell in Tandem: A Dual Absorber Artificial Leaf. *ACS Nano* **2015**, *9*, 11820–11829. [CrossRef] [PubMed]
56. McCrory, C.C.L.; Jung, S.; Peters, J.C.; Jaramillo, T.F. Benchmarking heterogeneous electrocatalysts for the oxygen evolution reaction. *J. Am. Chem. Soc.* **2013**, *135*, 16977–16987. [CrossRef] [PubMed]
57. McCrory, C.C.L.; Jung, S.; Ferrer, I.M.; Chatman, S.M.; Peters, J.C.; Jaramillo, T.F. Benchmarking Hydrogen Evolving Reaction and Oxygen Evolving Reaction Electrocatalysts for Solar Water Splitting Devices. *J. Am. Chem. Soc.* **2015**, *137*, 4347–4357. [CrossRef] [PubMed]
58. Pickrahn, K.L.; Park, S.W.; Gorlin, Y.; Lee, H.B.R.; Jaramillo, T.F.; Bent, S.F. Active MnO_x Electrocatalysts Prepared by Atomic Layer Deposition for Oxygen Evolution and Oxygen Reduction Reactions. *Adv. Energy Mater.* **2012**, *2*, 1269–1277. [CrossRef]
59. Jia, Q.; Iwashina, K.; Kudo, A. Facile fabrication of an efficient $BiVO_4$ thin film electrode for water splitting under visible light irradiation. *Proc. Natl. Acad. Sci. USA* **2012**, *109*, 11564–11569. [CrossRef] [PubMed]
60. Hernández, S.; Gerardi, G.; Bejtka, K.; Fina, A.; Russo, N. Evaluation of the charge transfer kinetics of spin-coated $BiVO_4$ thin films for sun-driven water photoelectrolysis. *Appl. Catal. B Environ.* **2016**, *190*, 66–74. [CrossRef]
61. Thalluri, S.M.; Rojas, R.M.; Rivera, O.D.; Hernandez, S.; Russo, N.; Rodil, S.E. Chemically induced porosity on $BiVO_4$ films produced by double magnetron sputtering to enhance the photo-electrochemical response. *Phys. Chem. Chem. Phys.* **2015**, *17*, 17821–17827. [CrossRef] [PubMed]

62. Thalluri, S.M.; Martinez Suarez, C.; Hussain, M.; Hernandez, S.; Virga, A.; Saracco, G.; Russo, N. Evaluation of the Parameters Affecting the Visible-Light-Induced Photocatalytic Activity of Monoclinic $BiVO_4$ for Water Oxidation. *Ind. Eng. Chem. Res.* **2013**, *52*, 17414–17418. [CrossRef]
63. Thalluri, S.M.; Martinez Suarez, C.; Hernández, S.; Bensaid, S.; Saracco, G.; Russo, N. Elucidation of important parameters of $BiVO_4$ responsible for photo-catalytic O_2 evolution and insights about the rate of the catalytic process. *Chem. Eng. J.* **2014**, *245*, 124–132. [CrossRef]
64. Hernández, S.; Thalluri, S.M.; Sacco, A.; Bensaid, S.; Saracco, G.; Russo, N. Photo-catalytic activity of $BiVO_4$ thin-film electrodes for solar-driven water splitting. *Appl. Catal. A Gen.* **2015**, *504*, 266–271. [CrossRef]
65. Ma, M.; Kim, J.K.; Zhang, K.; Shi, X.; Kim, S.J.; Moon, J.H.; Park, J.H. Double-deck Inverse Opal Photoanodes: Efficient Light Absorption and Charge Separation in Heterojunction. *Chem. Mater.* **2014**, *26*, 5592–5597. [CrossRef]
66. Berglund, S.P.; Rettie, A.J.E.; Hoang, S.; Mullins, C.B. Incorporation of Mo and W into nanostructured $BiVO_4$ films for efficient photoelectrochemical water oxidation. *Phys. Chem. Chem. Phys.* **2012**, *14*, 7065–7075. [CrossRef] [PubMed]
67. Luo, W.; Li, Z.; Yu, T.; Zou, Z. Effects of surface electrochemical pretreatment on the photoelectrochemical performance of Mo-doped $BiVO_4$. *J. Phys. Chem. C* **2012**, *116*, 5076–5081. [CrossRef]
68. Park, H.S.; Kweon, K.E.; Ye, H.; Paek, E.; Hwang, G.S. Factors in the Metal Doping of $BiVO_4$ for Improved Photoelectrocatalytic Activity as Studied by Scanning Electrochemical Microscopy (SECM) and First-Principles Density-Functional Calculation. *J. Phys. Chem. C* **2011**, *115*, 17870–17879. [CrossRef]
69. Jo, W.J.; Jang, J.W.; Kong, K.J.; Kang, H.J.; Kim, J.Y.; Jun, H.; Parmar, K.P.S.; Lee, J.S. Phosphate doping into monoclinic $BiVO_4$ for enhanced photoelectrochemical water oxidation activity. *Angew. Chem. Int. Ed.* **2012**, *51*, 3147–3151. [CrossRef] [PubMed]
70. Parmar, K.P.S.; Kang, H.J.; Bist, A.; Dua, P.; Jang, J.S.; Lee, J.S. Photocatalytic and photoelectrochemical water oxidation over metal-doped monoclinic $BiVO_4$ photoanodes. *ChemSusChem* **2012**, *5*, 1926–1934. [CrossRef] [PubMed]
71. Luo, W.; Yang, Z.; Li, Z.; Zhang, J.; Liu, J.; Zhao, Z.; Wang, Z.; Yan, S.; Yu, T.; Zhou, Z. Solar hydrogen generation from seawater with a modified $BiVO_4$ photoanode. *Energy Environ. Sci.* **2011**, *4*, 4046–4051. [CrossRef]
72. Jeong, H.W.; Jeon, T.H.; Jang, J.S.; Choi, W.; Park, H. Strategic modification of $BiVO_4$ for improving photoelectrochemical water oxidation performance. *J. Phys. Chem. C* **2013**, *117*, 9104–9112. [CrossRef]
73. He, H.; Berglund, S.P.; Rettie, A.J.E.; Chemelewski, W.D.; Xiao, P.; Zhang, Y.; Mullins, C.B. Synthesis of $BiVO_4$ nanoflake array films for photoelectrochemical water oxidation. *J. Mater. Chem. A* **2014**, *2*, 9371–9379. [CrossRef]
74. Yao, W.; Iwai, H.; Ye, J. Effects of molybdenum substitution on the photocatalytic behavior of $BiVO_4$. *Dalton Trans.* **2008**, 1426–1430. [CrossRef] [PubMed]
75. Thalluri, S.M.; Hernández, S.; Bensaid, S.; Saracco, G.; Russo, N. Green-synthesized W- and Mo-doped $BiVO_4$ oriented along the {040} facet with enhanced activity for the sun-driven water oxidation. *Appl. Catal. B Environ.* **2016**, *180*, 630–636. [CrossRef]
76. Pattengale, B.; Ludwig, J.; Huang, J. Atomic Insight into the W-Doping Effect on Carrier Dynamics and Photoelectrochemical Properties of $BiVO_4$ Photoanodes. *J. Phys. Chem. C* **2016**, *120*, 1421–1427. [CrossRef]
77. Gong, H.; Freudenberg, N.; Nie, M.; Van De Krol, R.; Ellmer, K. $BiVO_4$ photoanodes for water splitting with high injection efficiency, deposited by reactive magnetron co-sputtering. *AIP Adv.* **2016**, *6*, 45108. [CrossRef]
78. Monfort, O.; Sfaelou, S.; Satrapinskyy, L.; Plecenik, T.; Roch, T.; Plesch, G.; Lianos, P. Comparative study between pristine and Nb-modified $BiVO_4$ films employed for photoelectrocatalytic production of H_2 by water splitting and for the photocatalytic degradation of organic pollutants under simulated solar light. *Catal. Today* **2016**, *280*, 51–57. [CrossRef]
79. Wang, H.; Zhang, L.; Chen, Z.; Hu, J.; Li, S.; Wang, Z.; Liu, J.; Wang, X. Semiconductor heterojunction photocatalysts: Design, construction, and photocatalytic performances. *Chem. Soc. Rev.* **2014**, *43*, 5234–5244. [CrossRef] [PubMed]
80. Su, J.; Guo, L.; Bao, N.; Grimes, C.A. Nanostructured $WO_3/BiVO_4$ heterojunction films for efficient photoelectrochemical water splitting. *Nano Lett.* **2011**, *11*, 1928–1933. [CrossRef] [PubMed]

81. Murcia-López, S.; Fàbrega, C.; Monllor-Satoca, D.; Hernández-Alonso, M.D.; Penelas-Pérez, G.; Morata, A.; Morante, J.R.; Andreu, T. Tailoring Multilayered $BiVO_4$ Photoanodes by Pulsed Laser Deposition for Water Splitting. *ACS Appl. Mater. Interfaces* **2016**, *8*, 4076–4085. [CrossRef] [PubMed]
82. Zhang, L.; Reisner, E.; Baumberg, J.J. Al-doped ZnO inverse opal networks as efficient electron collectors in $BiVO_4$ photoanodes for solar water oxidation. *Energy Environ. Sci.* **2014**, *7*, 1402. [CrossRef]
83. Pilli, S.K.; Deutsch, T.G.; Furtak, T.E.; Brown, L.D.; Turner, J.A.; Herring, A.M. $BiVO_4/CuWO_4$ heterojunction photoanodes for efficient solar driven water oxidation. *Phys. Chem. Chem. Phys.* **2013**, *15*, 3273–3278. [CrossRef] [PubMed]
84. Rao, P.M.; Cai, L.; Liu, C.; Cho, I.S.; Lee, C.H.; Weisse, J.M.; Yang, P.; Zheng, X. Simultaneously Efficient Light Absorption and Charge Separation in $WO_3/BiVO_4$ Core/Shell Nanowire Photoanode for Photoelectrochemical Water Oxidation. *Nano Lett.* **2014**, *14*, 1099–1105. [CrossRef] [PubMed]
85. Liu, R.; Zheng, Z.; Spurgeon, J.; Yang, X. Enhanced photoelectrochemical water-splitting performance of semiconductors by surface passivation layers. *Energy Environ. Sci.* **2014**, *7*, 2504–2517. [CrossRef]
86. Eisenberg, D.; Ahn, H.S.; Bard, A.J. Enhanced Photoelectrochemical Water Oxidation on Bismuth. *J. Am. Chem. Soc.* **2014**, *136*, 14011–14014. [CrossRef] [PubMed]
87. Mcdowell, M.T.; Lichterman, M.F.; Spurgeon, J.M.; Hu, S.; Sharp, I.D.; Brunschwig, B.S.; Lewis, N.S. Improved Stability of Polycrystalline Bismuth Vanadate Photoanodes by Use of Dual-Layer Thin TiO_2/Ni Coatings. *J. Phys. Chem. C* **2014**, *118*, 19618–19624. [CrossRef]
88. Kim, T.W.; Choi, K.S. Improving Stability and Photoelectrochemical Performance of $BiVO_4$ Photoanodes in Basic Media by Adding a $ZnFe_2O_4$ Layer. *J. Phys. Chem. Lett.* **2016**, *7*, 447–451. [CrossRef] [PubMed]
89. Zhao, J.; Guo, Y.; Cai, L.; Li, H.; Wang, K.X.; Cho, I.S.; Lee, C.H.; Fan, S.; Zheng, X. High-Performance Ultrathin $BiVO_4$ Photoanode on Textured Polydimethylsiloxane Substrates for Solar Water Splitting. *ACS Energy Lett.* **2016**, *1*, 68–75. [CrossRef]
90. Qiu, Y.; Liu, W.; Chen, W.; Chen, W.; Zhou, G.; Hsu, P.; Zhang, R.; Liang, Z.; Fan, S.; Zhang, Y.; et al. Efficient solar-driven water splitting by nanocone $BiVO_4$-perovskite tandem cells. *Sci. Adv.* **2016**, *2*, e1501764. [CrossRef] [PubMed]
91. Arsenault, E.; Soheilnia, N.; Ozin, G.A. Periodic macroporous nanocrystalline antimony-doped tin oxide electrode. *ACS Nano* **2011**, *5*, 2984–2988. [CrossRef] [PubMed]
92. Long, X.; Li, J.; Xiao, S.; Yan, K.; Wang, Z.; Chen, H.; Yang, S. A strongly coupled graphene and FeNi double hydroxide hybrid as an excellent electrocatalyst for the oxygen evolution reaction. *Angew. Chem. Int. Ed.* **2014**, *53*, 7584–7588. [CrossRef] [PubMed]
93. Hernández, S.; Tortello, M.; Sacco, A.; Quaglio, M.; Meyer, T.; Bianco, S.; Saracco, G.; Pirri, C.F.; Tresso, E. New Transparent Laser-Drilled Fluorine-doped Tin Oxide covered Quartz Electrodes for Photo-Electrochemical Water Splitting. *Electrochim. Acta* **2014**, *131*, 184–194. [CrossRef]
94. Hernández, S.; Saracco, G.; Alexe-Ionescu, A.L.; Barbero, G. Electric investigation of a photo-electrochemical water splitting device based on a proton exchange membrane within drilled FTO-covered quartz electrodes: Under dark and light conditions. *Electrochim. Acta* **2014**, *144*, 352–360. [CrossRef]
95. Pinaud, B.A.; Benck, J.D.; Seitz, L.C.; Forman, A.J.; Chen, Z.; Deutsch, T.G. Technical and economic feasibility of centralized facilities for solar hydrogen production via photocatalysis and photoelectrochemistry. *Energy Environ. Sci.* **2013**, *6*, 1983–2002. [CrossRef]
96. Mckone, J.R.; Lewis, N.S.; Gray, H.B. Will Solar-Driven Water-Splitting Devices See the Light of Day? *Chem. Mater.* **2013**, *26*, 407–414. [CrossRef]
97. Bard, A.J.; Fox, M.A. Artificial Photosynthesis: Solar Splitting of Water to Hydrogen and Oxygen Water Splitting. *Acc. Chem. Res.* **1995**, *28*, 141–145. [CrossRef]
98. Park, H.S.; Lee, H.C.; Leonard, K.C.; Liu, G.; Bard, A.J. Unbiased photoelectrochemical water splitting in Z-scheme device using W/Mo-doped $BiVO_4$ and $Zn_xCd_{1-x}Se$. *ChemPhysChem* **2013**, *14*, 2277–2287. [CrossRef] [PubMed]
99. Toma, F.M.; Cooper, J.K.; Kunzelmann, V.; McDowell, M.T.; Yu, J.; Larson, D.M.; Borys, N.J.; Abelyan, C.; Beeman, J.W.; Yu, K.M.; et al. Mechanistic insights into chemical and photochemical transformations of bismuth vanadate photoanodes. *Nat. Commun.* **2016**, *7*, 12012. [CrossRef] [PubMed]
100. Artiphyction. Available online: http://www.artiphyction.org (accessed on 20 November 2016).
101. Gliozzi, A.S.; Hernández, S.; Alexe-Ionescu, A.L.; Saracco, G.; Barbero, G. A model for electrode effects based on adsorption theory. *Electrochim. Acta* **2015**, *178*, 280–286. [CrossRef]

102. Hernández, S.; Barbero, G.; Saracco, G.; Alexe-Ionescu, A.L. Considerations on oxygen bubble formation and evolution on $BiVO_4$ porous anodes used in water splitting photoelectrochemical cells. *J. Phys. Chem. C* **2015**, *119*, 9916–9925. [CrossRef]
103. Olateju, B.; Kumar, A. Techno-economic assessment of hydrogen production from underground coal gasification (UCG) in Western Canada with carbon capture and sequestration (CCS) for upgrading bitumen from oil sands. *Appl. Energy* **2013**, *111*, 428–440. [CrossRef]